Atmospheric
Measurement
Techniques

# Sensitivity analysis of polarimetric $O_2$ A-band spectra for potential cloud retrievals using OCO-2/GOSAT measurements

S. Sanghavi[1,2], M. Lebsock[1], and G. Stephens[1,2]

[1]Jet Propulsion Laboratory, California Institute of Technology, Pasadena, USA
[2]Department of Atmospheric Science, Colorado State University, Fort Collins, USA

*Correspondence to:* S. Sanghavi (suniti.v.sanghavi@jpl.nasa.gov)

**Abstract.** Clouds play a crucial role in Earth's radiative budget, yet their climate feedbacks are poorly understood. The advent of space-borne high resolution spectrometers probing the $O_2$ A band, like GOSAT and OCO-2, could make it possible to simultaneously retrieve vertically resolved cloud parameters that play a vital role in Earth's radiative budget, thereby allowing a reduction of the corresponding uncertainty due to clouds. Such retrievals would also facilitate air mass bias reduction in corresponding measurements of $CO_2$ columns.

In this work, the hyperspectral, polarimetric response of the $O_2$ A band to mainly three important cloud parameters, viz., optical thickness, top height and droplet size has been studied, revealing a different sensitivity to each for the varying atmospheric absorption strength within the A band. Cloud optical thickness finds greatest sensitivity in intensity measurements, the sensitivity of other Stokes parameters being limited to low cloud optical thicknesses. Cloud height had a negligible effect on intensity measurements at non-absorbing wavelengths but finds maximum sensitivity at an intermediate absorption strength, which increases with cloud height. The same is found to hold for cloud geometric thickness. The geometry-dependent sensitivity to droplet size is maximum at non-absorbing wavelengths and diminishes with increasing absorption strength. It has been shown that significantly more information on droplet size can be drawn from multi-angle measurements. We find that, in the absence of sunglint, the backscatter hemisphere (scattering angle larger than 90°) is richer in information on droplet size, especially in the glory and rainbow regions. It has been shown that $I$ and $Q$ generally have differing sensitivities to all cloud parameters. Thus, accurate measurements of two or-
thogonal components $I_P$ and $I_S$ (as in GOSAT) are expected to contain more information than measurements of only $I$, $I_h$ or $I_v$ (as in the case of OCO-2).

## 1 Introduction

In the context of satellite-based remote sensing, the $O_2$ A band has long been regarded a rich source of information on the vertical structure of scattering in Earth's atmosphere (Fischer and Grassl, 1991; Fischer et al., 1991; O'Brien and Mitchell, 1992; Pfeilsticker et al., 1998; Heidinger and Stephens, 2000; Koelemeijer et al., 2001; Rozanov and Kokhanovsky, 2004; Van Diedenhoven et al., 2007). The $O_2$ A band consists of lines of absorption that span a range of optical thickness covering several orders of magnitude in Earth's atmosphere. Strongly absorbing lines cause rapid extinction of light and shorter atmospheric path lengths, whereas weaker lines are associated with longer path lengths. Since the $O_2$ mixing ratio can be assumed constant for remote sensing purposes, it makes absorption due to $O_2$ at different wavelengths in the A band a good proxy for the geometric depth within the atmosphere to which most of the incident light could penetrate before being either scattered or getting absorbed.

In addition to the influence of atmospheric absorption, the scattered light is also affected by the properties of the scattering medium. In the case of liquid water clouds, the Stokes vector of the scattered light in an absorbing atmosphere is a function of cloud optical thickness, cloud top height and the size of its constituent droplets (Kokhanovsky, 2006). Cloud microphysics is critical to understanding the hydrological

cycle (Chahine, 1992; Fowler et al., 1996; Baker, 1997). Droplet size affects cloud brightness (Lohmann and Feichter, 1997; Peng and Lohmann, 2003; Lohmann et al., 2007), thus affecting its ability to reflect back incident solar irradiation. Cloud height also impacts the nature of its radiative feedback (Stephens and Platt, 1987; Slingo and Slingo, 1988; Slingo, 1990; Stephens et al., 2002; Stephens, 2005). The determination of cloud microphysics generally involves the use of thermal infrared and microwave measurements in addition to those in the visible and near infrared ranges (Nakajima and King, 1990; Nakajima et al., 1991; Nakajima and Nakajma, 1995; Platnick and Valero, 1995). Attempts to determine the height of clouds generally involve strong absorption bands (Kuze and Chance, 1994; Rozanov et al., 2004; Sanghavi et al., 2012) or lidar techniques (Dessler et al., 2006; Sassen et al., 2008). The main goal of this work is to examine the cloud information content of the A band using simple simulations, by taking into account not only the intensity but also the polarization of the scattered radiation. The effect of potential multi-angular measurements on the determination of cloud droplet size is also probed.

Given that the O$_2$ A band is peculiar in that it displays a sensitivity to scattering at different depths of the atmosphere by virtue of several lines of varying absorption strengths, we first examine the effect of column absorption strength in Sect. 2 and the microphysics of the scattering cloud in Sect. 3. In Sect. 4, the behavior of the scattered intensity as well as the degree of polarization in response to changes in cloud height (Sect. 4.2), cloud droplet size (Sect. 4.3) and cloud optical thickness (Sect. 4.1) is examined using simulated measurements. In addition to the influence of cloud height, the effect of cloud geometric thickness is also investigated in Sect. 4.2.1. Also, the gain in information on droplet size using multi-angle polarized measurements is studied in Sect. 4.3.1. Section 5 identifies characteristic differences in the sensitivity of the O$_2$ A band to different cloud parameters, which can be used in an optimized inversion setup to retrieve them simultaneously.

The relevance of our findings to observations made by the GOSAT (Greenhouse gases Observing SATellite; Hamazaki et al., 2005; Kuze et al., 2009) instrument and the recently launched OCO-2 (Orbiting Carbon Observatory-2; Crisp et al., 2004; Pollock et al., 2010) instrument has been pointed out in our concluding remarks in Sect. 6, in view of the fact that both instruments provide hyperspectral measurements of the O$_2$ A band, with a spectral resolution of about 0.04 nm, in addition to measurements of the weak and strong CO$_2$ bands centered around 1.6 and 2.06 nm, respectively. Polarization is included in both instruments, albeit only in the form of $I_h = \frac{1}{2}(I + Q)$ in the case of OCO-2, while GOSAT measures two orthogonal components, $I_P$ and $I_S$, each being a view geometry-dependent linear combination of the elements of the Stokes vector of the measured signal (O'Brien et al., 2013). The ability for multi-angle measurements is available to a limited extent in both instruments: GOSAT provides a range of view angles due to its pointing mechanism which covers $\pm 35°$ across track and $\pm 20°$ along track, while OCO-2 periodically employs its target mode, during which it is expected to lock its view onto a specific surface location and retain that view while flying overhead. Over the 9 min time period of a target track pass, OCO-2 can acquire up to 12 960 measurements at local zenith angles that vary between 0 and $\pm 85°$, thus providing a good angular coverage over the ground pixel. (Note: in the target mode, OCO-2 measurements are no longer limited to the principal plane, and are thus a linear combination of the Stokes components $I$, $Q$ and $U$, where the coefficients for each component are given by a Mueller matrix whose elements depend on the angle between the slit and the principal plane.) While it is clear that OCO-2/GOSAT may not match the full capabilities of dedicated instruments like CloudSat (Stephens et al., 2008), MODIS (Moderate Resolution Imaging Spectroradiometer; Ackerman et al., 2008), AVHRR (Advanced Very High Resolution Radiometer; Key and Barry, 1989), MERIS (MEdium Resolution Imaging Spectrometer; Gómez-Chova et al., 2006), etc., the high spectral resolution of the O$_2$ A band does provide the benefit of unprecedented vertical resolution combined with sensitivity to particle size because of the large spectral range covered. Exploring the information content of these measurements to cloud retrievals also opens the possibility of synergistic retrievals with other instruments.

The following section starts with an examination of the vertical sensitivity to the column absorption strength of the atmosphere within the O$_2$ A band.

## 2   Vertical sensitivity of the O$_2$ A band

The absorption cross section, $\sigma_{abs}$, of O$_2$ at a given wavelength $\lambda$ varies with height $z$ as a function of pressure and temperature. Using climatological temperature and pressure profiles of a mid-latitude summer and line parameters from the HITRAN (High Resolution Transmission) 2008 database (Rothman et al., 2009), we obtain total column optical thicknesses in the O$_2$ A band (plotted along the right ordinate of Fig. 1 at a spectral resolution of 0.005 nm). For the purpose of this sensitivity study, the HITRAN database and a Voigt line shape are sufficient, but line-mixing effects have to be taken into consideration for retrievals with real data (Tran and Hartmann, 2008). Furthermore, the Rayleigh optical thickness has been assumed to be fixed throughout the O$_2$ A band at its value at 760 nm.

To determine the response of the individual lines to the depth of scattering of solar irradiation, we assume a white laminar plate (WLP) of infinite horizontal extent featuring Lambertian reflectance (plane albedo $\omega_0 = 1$) at a height $z$ above the ground surface. For a wavelength $\lambda$, the response, $s_{WLP}(\lambda, z)$, to scattering at this plate is proportional to the amount of light transmitted to the plate (assuming no significant scattering above the surface):

$$s_{\text{WLP}}(\lambda, z) \propto T(z; \mu, \mu_0) = \exp\{-\tau_\lambda(z)/\overline{\mu}\}, \quad (1)$$

where

$$\frac{1}{\overline{\mu}} = \frac{1}{\mu_0} + \frac{1}{\mu}, \quad (2)$$

$\mu_0$ and $\mu$ represent the cosines of the solar and view zenith angles, and $\tau_\lambda(z)$ represents the optical thickness of absorption above the WLP. With a constant of proportionality $\frac{1}{\pi}$ given by the conservation of flux, we get a response,

$$s_{\text{WLP}}(\lambda, z) = \frac{1}{\pi} \exp\left\{-\frac{\tau_\lambda(z)}{\overline{\mu}}\right\}, \quad (3)$$

for the geometry under consideration. Neglecting for simplicity the variation of the absorption cross section $\sigma_{\text{abs}}(\lambda)$ with height, the exponentially decreasing vertical profile of $O_2$ allows us to use the following relation for the absorption optical depth of $O_2$ at an atmospheric level $z$:

$$\tau_\lambda(z) = \tau_{\text{abs},0}(\lambda) \exp(-z/H), \quad (4)$$

where $\tau_{\text{abs},0}(\lambda)$ is the total column optical depth of absorption due to $O_2$ at wavelength $\lambda$ and $H \approx 8\,\text{km}$ is the scale height. Substituting Eq. (4) in Eq. (3), and expressing the optical depth as a function of wavelength, $\lambda$, yields the response at $\lambda$ of light reflected at height $z$ in the atmosphere:

$$s_{\text{WLP}}(z, \lambda) = \frac{1}{\pi} \exp\left\{-\frac{\tau_{\text{abs},0}(\lambda)}{\overline{\mu}} \exp(-z/H)\right\}, \text{ or}$$

$$s_{\text{WLP}}(z, \tau_{\text{abs},0}) = \frac{1}{\pi} \exp\left\{-\frac{\tau_{\text{abs},0}}{\overline{\mu}} \exp(-z/H)\right\}, \quad (5)$$

where the second line expresses $s_{\text{WLP}}$ as a function of $z$ and $\tau_{\text{abs},0}$, with an implicit dependence on $\lambda$ through the latter.

This bivariate sensitivity to $z$ and $\tau_{\text{abs},0}$ is depicted along the $z$ axis of Fig. 2 for a nadir-viewing geometry with the Sun at zenith ($\mu_0 = \mu = 1$), as a function of height along the $x$ axis and atmospheric absorption along the $y$ axis. The top-of-atmosphere (TOA) can be defined as the height above the surface where the molecular concentration becomes negligible (and thus $\tau_{\text{abs}}(\lambda) \to 0$ for all $\lambda$). Thus, Eq. (3) yields the response $s_{\text{WLP}} \to 1/\pi$ for all $\tau_{\text{abs},0}$ at $z \to$ TOA and for all $z$ at $\tau_{\text{abs},0} \to 0$. Thus, it is evident that the non-absorbing atmosphere is equally sensitive at all heights, since atmospheric scattering has been assumed negligible. (This assumption can be expected to approximate the sensitivity of a Rayleigh scattering atmosphere in the $O_2$ A band due to the low optical thickness of Rayleigh scattering in this spectral region: $\tau_{\text{Rayl}}(765\,\text{nm}) = 2.5433 \times 10^{-2}$ (Bodhaine et al., 1999).) With increasing absorption, however, the reflected light shows increasingly lower sensitivity to layers closer to the surface. Thus, at $\tau_{\text{abs},0} \approx 40$, there is practically no sensitivity to reflection at levels as high as 20–25 km above the surface.
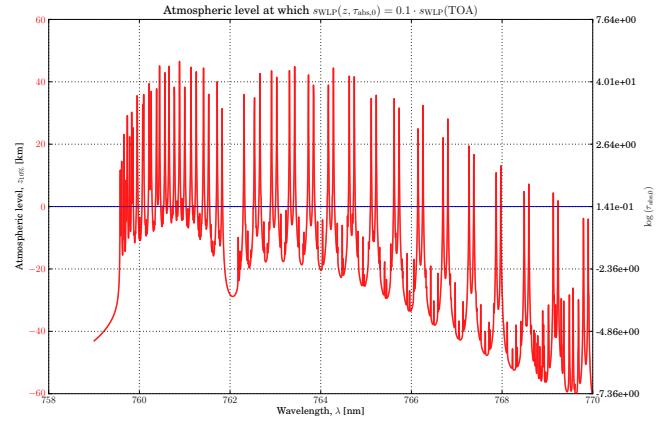


**Figure 1.** The atmospheric height (red) above the surface at which the reflectance is expected to be reduced to $s_{\text{WLP}} = 0.032$ or about 10 % of the sensitivity at the top of atmosphere (TOA). Negative heights are unphysical (below the surface) and indicate that all atmospheric levels above the surface are more sensitive than $s = 0.032$. This height is directly proportional to the logarithm of the total absorption optical thickness, shown along the right ordinate.

By setting a cutoff at $s_{\text{WLP}}^{\text{c}}$, it is possible to estimate the minimum height $z_{\min}$ up to which the atmosphere is sensitive to reflection at a given wavelength $\lambda$. Setting $s_{\text{WLP}} = s_{\text{WLP}}^{\text{c}}$ in Eq. (5) and rearranging the terms yields

$$z_{\min}(\lambda) = H\left[\ln\left(\tau_{\text{abs},0}(\lambda)\right) - \ln\left(-\overline{\mu}\ln(\pi \cdot s_{\text{WLP}}^{\text{c}})\right)\right]$$

$$= H\left[\ln\left(\tau_{\text{abs},0}(\lambda)\right) - \ln\left(-\overline{\mu}\ln\left(\frac{s_{\text{WLP}}^{\text{c}}}{s_{\text{WLP}}(\text{TOA})}\right)\right)\right], \quad (6)$$

since $s_{\text{WLP}}(\text{TOA}) = \frac{1}{\pi}$. The above equation has the linear form $z_{\min}(\lambda) = m \cdot \ln\left(\tau_{\text{abs},0}(\lambda)\right) + c$, where $m = H$ and $c = -H\ln\left(-\overline{\mu}\ln\left(\frac{s_{\text{WLP}}^{\text{c}}}{s_{\text{WLP}}(\text{TOA})}\right)\right)$. This is illustrated by Fig. 1, which shows $z_{\min}$ on the left over the A band for a cutoff sensitivity of about 10 % of $s_{\text{WLP}}(\text{TOA})$ at $s_{\text{WLP}}^{\text{c}} = 0.1/\pi$, with the corresponding value of $\log(\tau_{\text{abs},0})$ shown along the right ordinate. It can be verified that both ordinate scales in the figure are linear, as required by Eq. (6). The geometry assumed is the same as for Fig. 2, viz., $\mu_0 = \mu = 1$. Negative values of $z_{\min}$ indicate that the entire atmospheric column is more sensitive to reflectance than $s_{\text{WLP}}^{\text{c}}$. Equation (6) shows that this occurs when the column absorption falls below the following critical value:

$$\tau_{\text{abs},0}(\lambda) \leq -\overline{\mu}\ln\left(\frac{s_{\text{WLP}}^{\text{c}}}{s_{\text{WLP}}(\text{TOA})}\right). \quad (7)$$

Thus, for the geometry $\mu_0 = \mu = 1$, the entire atmospheric column has sensitivity $s > 0.1 \cdot s_{\text{TOA}}$ to reflectance when the column optical thickness is less than a critical value of $\tau_{\text{abs},0}^{\text{c}} \approx 1.15$ or $\log(\tau_{\text{abs},0}^{\text{c}}) = 0.141$, corresponding to $z_{\min} = 0$ as can be seen in Fig. 1. (For geometries other than the one considered here, $\tau_{\text{abs},0}^{\text{c}} \approx 2.30 \cdot \overline{\mu}$.)
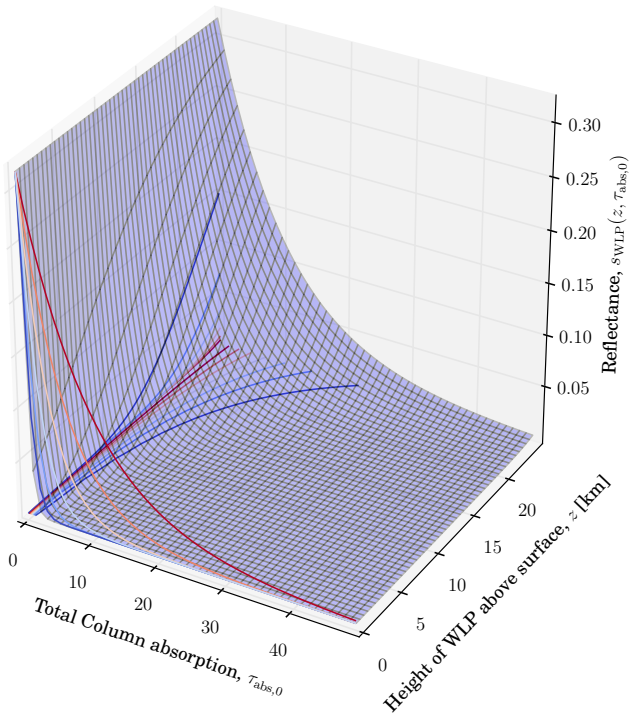
**Figure 2.** Sensitivity $s$ to Lambertian laminar reflectance of albedo $\omega_0 = 1$ at height $z$ above a black surface in a purely absorbing atmosphere ($\theta_{Sun} = \theta_{View} = 0$) as a function of total column absorption strength, $\tau_{abs,0}$ (assuming an exponential concentration profile of scale height $H = 8$ and uniform absorption cross section at all levels).

The differential sensitivities to $z$ of absorption lines measurably affect the spectral signature of backscattered light and thus contribute substantially to the information content of the $O_2$ A band on the vertical distribution of scattering species like clouds and aerosol. In the extreme limit, strongly absorbing lines such as those near 760.885 nm ($\tau_{abs,0}(760.885\ nm) = 386.48$) and 760.445 nm ($\tau_{abs,0}(760.445\ nm) = 322.92$) are saturated long before the light can penetrate the atmosphere to levels where clouds or aerosols can be expected, rendering them practically useless for the purpose of providing vertical information. Thus, the R branch of the $O_2$ A band (centered roughly around 761 nm), which is much more densely populated by strong absorption lines than the P branch (centered around $\approx 764$ nm), exhibits comparatively reduced sensitivity to lower atmospheric scattering heights.

The above discussion assumed a white Lambertian reflecting surface at a given atmospheric level. While this allows us to study the nature of the individual lines constituting the $O_2$ A band, it does not suffice to describe backscattering by atmospheric clouds, which have to be represented by a vertical distribution (ignoring variations in the two horizontal dimensions) and as a distribution of differently sized droplets. In the following section, we explore the scattering characteris-

tics of a water cloud as a function of the size of its constituent droplets.

## 3  Dependence of the scattering properties of clouds on droplet size

The Mie theory (van de Hulst, 1957; Deirmendjian, 1969; Wiscombe, 1980; Bohren and Huffman, 1983) allows us to determine the dependence of the single scattering properties of a scattering particle as a function of size.

The extinction efficiency $\kappa$ approaches the asymptotic value of 2 as $x \rightarrow \infty$. Thus, for larger droplets typical of clouds, the extinction cross section is approximately $C_{ext} = 2\pi r^2$. The single scattering albedo of a given droplet varies only very slightly beyond $x = 50$–$100$. Thus, for a droplet of size $r$, the single scattering albedo is practically constant for all wavelengths smaller than $\lambda \approx \frac{2\pi r}{75}$, which is reflected in the white appearance of clouds.

We have considered pure water clouds ($n = 1.33 - 0.0\iota$) consisting of droplets represented by lognormal size distributions of width $\sigma_0 = 1.13$ (chosen to comply roughly with the findings of Nakajima et al. (2010); Mayer et al. (2004); Stephens and Platt (1987); Stephens (1978)) around five different median radii, $r_0 = 5, 7.5, 10, 12.5$ and $15$ nm, as shown in the top panel of Fig. 3. The lognormal distribution is defined in terms of the probability $\rho(r)dr$ of finding a droplet in the size interval $[r, r + dr]$ such that

$$\rho(r)dr = \frac{1}{\sqrt{2\pi} r \log(\sigma_0)} \exp\left[-\frac{(\log(r) - \log(r_0))^2}{2\log^2(\sigma_0)}\right] dr. \quad (8)$$

An assumption of a constant cloud optical thickness $\tau = N(r_0)C_{ext}(r_0)\Delta z$ within the same geometric thickness, $\Delta z$, leads to an inverse relation between the number density $N(r_0)$ and the extinction cross section $C_{ext}(r_0)$ as shown in the bottom panel of Fig. 3. Thus, the choice of a homogenous pure cloud of constant optical thickness eliminates any size dependence of the scattered light due to $C_{ext}$ or $\omega_0$. The only property determining the scattering of light as a function of size is thus reduced to the phase matrix $\mathbf{P}(\theta_{scatt})$.

Fig. 4 shows the phase functions $P_v(\theta_{scatt})$ and $P_h(\theta_{scatt})$ governing the scattering of the orthogonal components $I_v = \frac{1}{2}(I - Q)$ and $I_h = \frac{1}{2}(I + Q)$ of the modified Stokes vector, respectively. The features of the phase matrix are most evident in the component of scattered light that has undergone only one scattering event (the single-scatter component). This is true both for the polarization as well as the angular dependence of the scattered light. As the order of scattering increases due to multiple scattering, the radiation field becomes more and more isotropic, thus losing much of the angular form of the original phase matrix.

In the following section, the vertical sensitivity of absorption lines discussed in Sect. 2 as well as the size dependence of the measurement through the phase function of the cloud droplets discussed above are used to closely examine the ef-
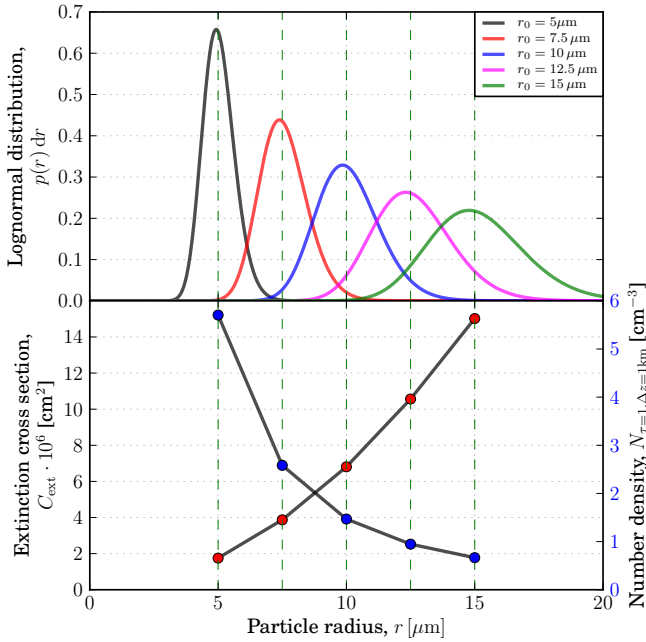
**Figure 3.** Top panel: lognormal droplet size distributions for median radii $r_0 = 5$, 7.5, 10, 12.5 and 15 µm, respectively, each with a width $\sigma_0 = 1.13$. Bottom panel: extinction cross section $C_{\text{ext}}$ (cm$^2$) (red) of each size distribution (left) and the corresponding number density $N$ (droplets cm$^{-3}$) (blue) for a constant cloud optical thickness $\tau = 1$ and a geometric thickness $\Delta z = 1$ km.



**Figure 4.** Phase functions $P_{\text{h}}(\theta_{\text{scatt}})$ and $P_{\text{v}}(\theta_{\text{scatt}})$ as a function of scattering angle $\theta_{\text{scatt}}$ for distributions with median radii $r_0 = 5$, 7.5, 10, 12.5 and 15 µm, respectively, each with a width $\sigma_0 = 1.13$. The refractive index in each case is $n = 1.33 - 0.0\iota$. The dashed line shows the corresponding Rayleigh scattering phase functions.

fects of droplet size, cloud height, cloud optical thickness and cloud geometric thickness on the intensity and polarization of scattered light within the O$_2$ A band.

## 4 Sensitivity of the O$_2$ A band to cloud parameters

We use the vector radiative transfer model vSmartMOM (Sanghavi et al., 2014) implementing a corr-k approach similar to that of Hasekamp and Butz (2008) using HITRAN 2008 (Rothman et al., 2009) spectral data for modeling O$_2$ A-band absorption. Climatological vertical profiles of temperature and pressure are adapted from the MODTRAN database (MODerate resolution atmospheric TRANsmission; Abreu and Anderson, 1996; Anderson et al., 1986) for the computation of the absorption cross sections. The Stokes vector $\mathbf{I} = [I, Q, U, V]$ (scattered radiance normalized with respect to the solar flux) is computed at a spectral resolution of 0.005 nm over the range 759–770 nm for a nadir-viewing geometry. Hyperspectral simulations are subsequently convolved with a Gaussian slit function of FWHM (full width at half maximum) at 0.04 nm representative of the OCO-2 and GOSAT instruments. The Sun is assumed to be at an angle $\theta_0 = 60°$ from the zenith, and Earth's surface is assumed to be black. Cloud coverage is assumed to be 100 %. Computations of the reflected vector $\mathbf{I}$ have been made for cloud optical thickness $\tau_{\text{cloud}} = 1.0$, 5.0, 10.0 and 50.0. The cloud ge-
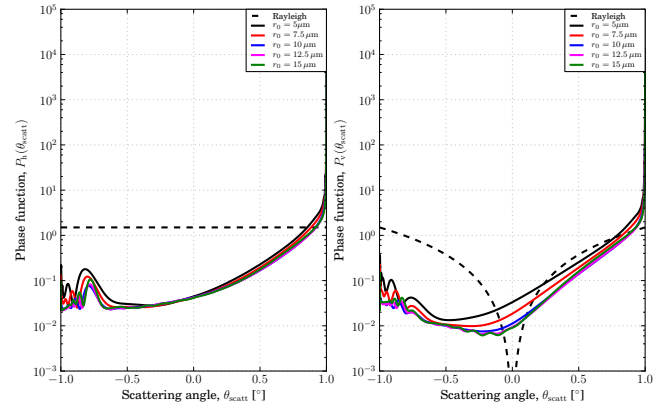
ometric thickness $\Delta z$ is assumed to be 400 m, within which the cloud is assumed to be uniformly distributed. The cloud top, however, is varied between 2.4 and 12.4 km at intervals of 2 km, i.e., $z_{\text{top}} = 2.4$, 4.4, 6.4, 8.4, 10.4, and 12.4 km. To analyze the reflected intensity $I$ and the Stokes component $Q$ of the O$_2$ A band, we consider for reference

1. a clear-sky atmosphere consisting of only molecular scatterers, and

2. a white Lambertian plate (WLP), as considered in Sect. 2, at a height of $z = 6.4$ km above the surface,

and compare its response with that due to the presence of

1. a cloud of constant geometric thickness, $\Delta z = 400$ m, size distribution parameter, $r_0 = 10$ µm, and cloud top height $z_{\text{top}} = 6.4$ km, but varying cloud optical thicknesses $\tau_{\text{cloud}}$ as in Fig. 5;

2. a cloud of constant optical thickness, $\tau_{\text{cloud}} = 10$, geometric thickness, $\Delta z = 400$ m, and size distribution parameter $r_0 = 10$ µm, but varying cloud top heights $z_{\text{top}}$ as shown in Fig. 6; and

3. a cloud of constant optical thickness, $\tau_{\text{cloud}} = 10$, geometric thickness, $\Delta z = 400$ m, and cloud top height $z_{\text{top}} = 6.4$ km, but varying cloud median droplet radii $r_0$ as shown in Fig. 7.

Figures 6, 7 and 5, each show simulated measurements of the reflected intensity $I$ and the Stokes parameter $Q$ ($U = V = 0$ in a nadir-viewing geometry) in the top and bottom panels, respectively, with each quantity plotted against wavelength on the left and total column absorption on the right. The dependence of both $I$ and $Q$ on $\tau_{\text{abs},0}$ is expected to be

$$r_0 = 10 \, \mu\text{m}, \; z_{\text{top}} = 6.4 \text{ km}, \; \Delta z = 400 \text{ m}$$
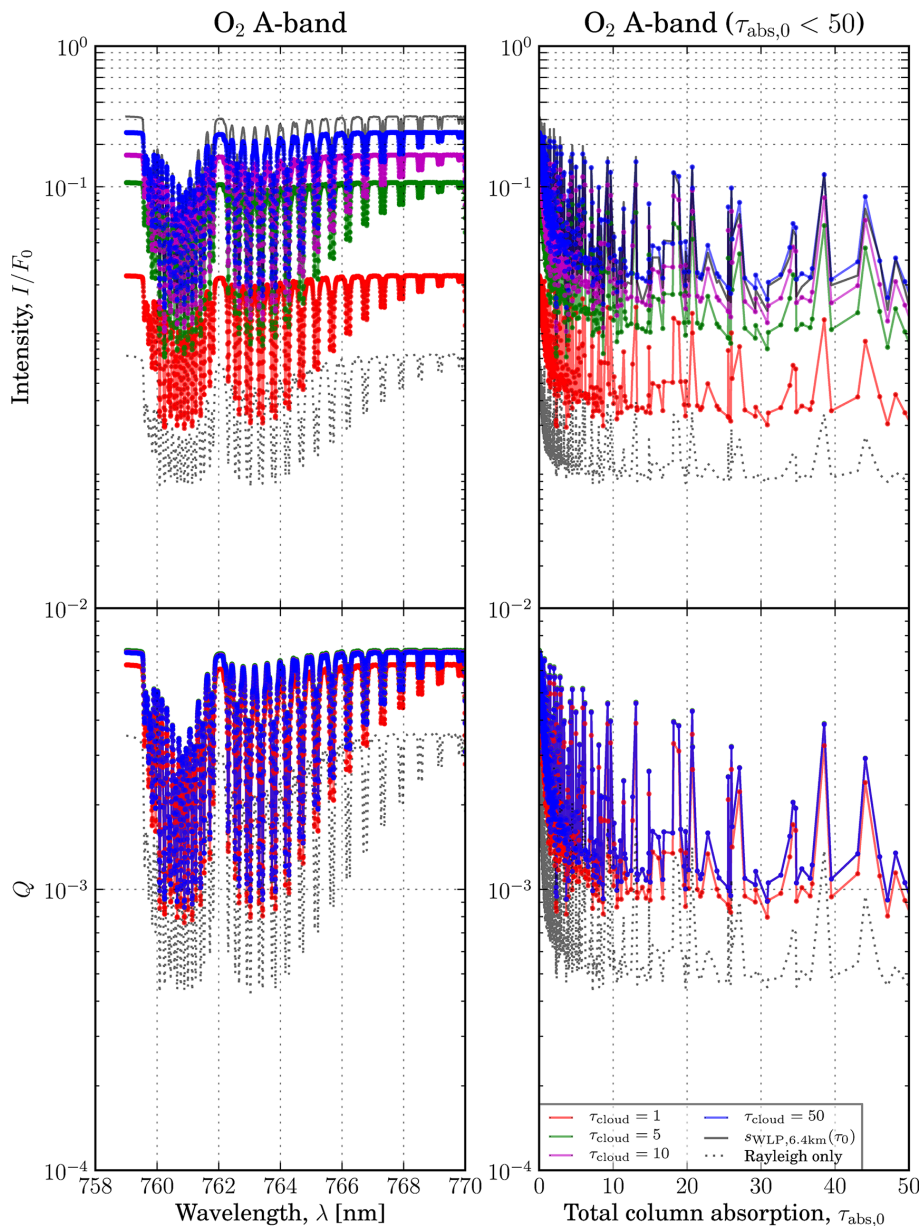


**Figure 5.** Intensity (top) and degree of polarization (bottom) due to a cloud-laden atmosphere of constant cloud droplet size, $r_0 = 10 \, \mu\text{m}$, at a top height of $z_{\text{top}} = 10.4$ km but varying cloud optical thickness $\tau_{\text{cloud}}$ in the $O_2$ A band.

monotonic. Deviations from the monotonicity are observed primarily because of convolution, which causes a spread of absorption strength from the individual lines to the neighboring wavelengths. A weaker role is played by the vertical variation of absorption cross section of $O_2$, which disturbs a 1 : 1 relationship between the total column absorption strength and the measured value of $I$ or $Q$.

For a given absorption strength, in general, higher reflected intensities $I$ are indicative of higher isotropicity of the single scattering phase function and/or increased single/multiple scattering. In contrast, the polarization signal $Q$ is only sensitive to the first few orders of scattering undergone by the incident flux (Schutgens et al., 2004). $Q = I_{\text{h}} - I_{\text{v}}$ becomes increasingly diminished for higher orders of scattering due to the blurring of the differences between the components $I_{\text{h}}$ and $I_{\text{v}}$. This is because each new scattering event involves a different scattering plane and, consequently, a different rotation of the scattering matrix according to Hovenier (1971).

$\tau_{\mathrm{cloud}} = 10$, $r_0 = 10\,\mu\mathrm{m}$, $\Delta z = 400\,\mathrm{m}$
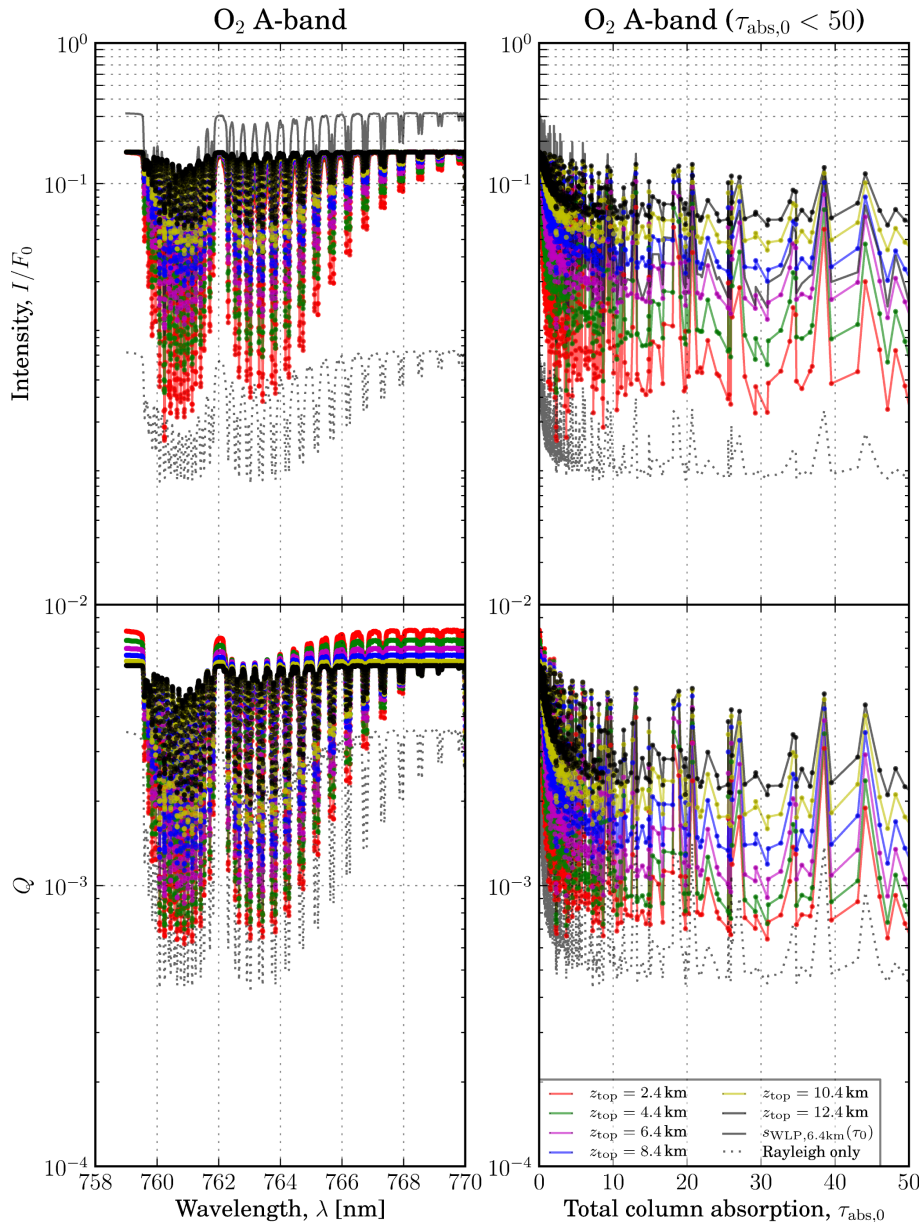


**Figure 6.** Intensity (top) and degree of polarization (bottom) due to a cloud-laden atmosphere of constant cloud optical depth, $\tau_{\mathrm{cloud}} = 10$, with a median droplet radius of $r_0 = 10\,\mu\mathrm{m}$ but varying cloud $z_{\mathrm{top}}$ (but constant geometric thickness $\Delta z = 400\,\mathrm{m}$) in the $O_2$ A band.

## 4.1 Sensitivity to cloud optical thickness

The upper left panel of Fig. 5 shows that the greatest difference between the pure molecular (dashed black line) and cloudy atmospheres is the increase in reflected intensity, attributable to increases in both single and multiple scattering at all column absorption strengths, as can be verified in the upper right panel. The reflected intensity due to the WLP at $z = 6.4\,\mathrm{km}$ (solid black line), however, only serves

as an upper bound at $I = 1/\pi$ near $\tau_{\mathrm{abs},0} = 0$. With increasing $\tau_{\mathrm{abs},0}$, the reflected intensity reaches a more or less steady level slightly below that due to the cloud of optical thickness $\tau_{\mathrm{cloud}} = 50$. This is likely caused by the presence of molecular scatterers above $6.4\,\mathrm{km}$ in the cloudy cases, which have not been considered in the WLP case. The upper panels also show that the reflected intensity increases with increasing cloud optical thickness, albeit at a steadily decreasing rate.

$\tau_{\mathrm{cloud}} = 10$, $z_{\mathrm{top}} = 6.4$ km, $\Delta z = 400$ m
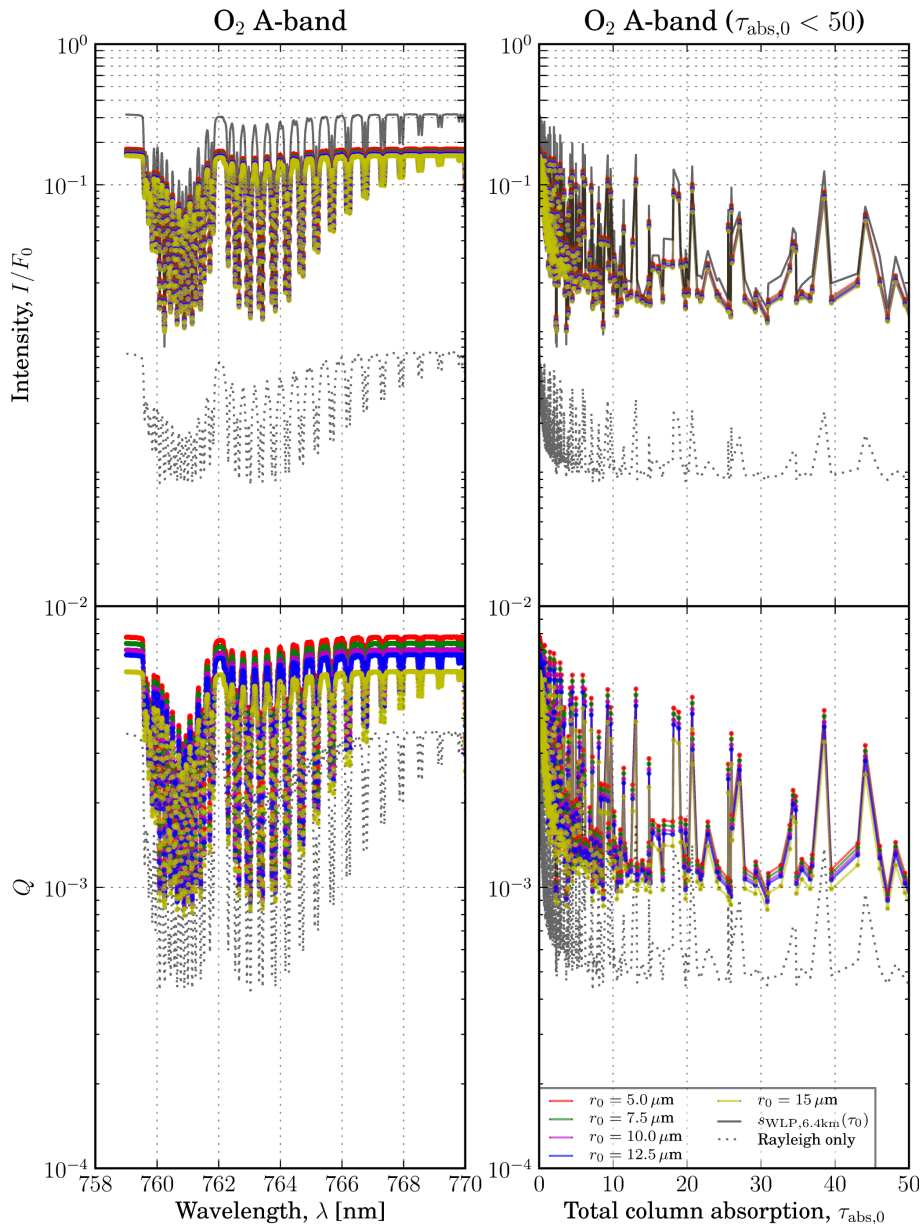


**Figure 7.** Intensity (top) and degree of polarization (bottom) due to a cloud-laden atmosphere of constant cloud optical depth, $\tau_{\mathrm{cloud}} = 10$ at a top height of $z_{\mathrm{top}} = 6.4$ km but varying median cloud droplet radii in the O$_2$ A-band.

While the increase in intensity with increasing $\tau_{\mathrm{cloud}}$ is caused by increases in single as well as (more predominantly) multiple scattering, $Q$ is mainly affected only by the lowest orders of scattering. As a result, we see practically no change in $Q$ beyond $\tau_{\mathrm{cloud}} = 5$ after an initial increase due to increasing single scattering. For the geometry considered, $Q$ is bounded below by Rayleigh scattering at all wavelengths, while the WLP has no contribution to $Q$ due to its Lambertian nature.

## 4.2 Sensitivity to cloud height

Similar to the previous case in which varying cloud optical thicknesses were considered, the upper left panel of Fig. 6 shows the reflected intensity $I$ due to clouds of varying heights. Again, the pure molecular case (dashed black line) provides a lower bound, while the WLP at $z = 6.4$ km is an upper bound at $\tau_{\mathrm{abs},0} = 0$ (solid black line). The reflected intensity $I$ is seen to show no sensitivity to cloud

height at $\tau_{abs,0} = 0$ but clearly shows a height-dependent response at $\tau_{abs,0} > 0$. The upper right panel shows that high clouds reflect more than low clouds for a given finite absorption strength, as the former cause more previously unscattered light to be intercepted by cloud droplets, preventing it from penetrating deeper into the atmosphere where it can undergo more absorption due to the higher concentration of $O_2$ molecules. The response of the WLP (solid black line) at $z = 6.4$ km falls rapidly from $I = 1/\pi$ with increasing $\tau_{abs,0}$ and assumes a steady value between that of clouds at $z_{top} = 6.4$ km (purple) and $z_{top} = 8.4$ km (blue). The difference between the response of the WLP and cloud at $z_{top} = 6.4$ km for finite $\tau_{abs,0}$ can be explained as follows.

1. The white plate is solid with an albedo of 1, reflecting all the light incident on it, while the cloud has a lower albedo, as some of the light incident on it is also transmitted to lower atmospheric layers. As a result, for most geometries, the WLP leads to more reflected intensity than the cloud of optical thickness 10 at the same top height.

2. The cloud has a finite extent (400 m) below its top at 6.4 km, as a result of which some of the light is reflected back at lower atmospheric levels than $z_{top}$, allowing more absorption. All the light incident on the WLP is reflected at exactly $z = 6.4$ km, so that no further absorption is possible.

3. The WLP is the only scatterer, whereas there exists molecular (Rayleigh) scattering throughout the atmospheric column in addition to the cloud. This leads to a positive contribution due to both more single and multiple scattering, which however is not sufficient to compensate for the albedo of the WLP for a cloud optical thickness of 10 (Fig. 5 shows, however, that this contribution is more significant at $\tau_{cloud} = 50$).

While $I$ shows practically no sensitivity to $z_{top}$ in the absence of absorption, the lower left and right panels show a high sensitivity of $Q$ to cloud top height at all $\tau_{abs,0}$ considered in Fig. 6. Higher clouds shield larger sections of the atmospheric column, reflecting light before it can interact with the molecules below it. As a result, low-order Rayleigh scattering occurs to a lesser extent with increasing cloud height. The relatively strong polarization due to Rayleigh scattering in the given geometry thus gives rise to a significant sensitivity of $Q$ to $z_{top}$ for $\tau_{abs,0} \geq 0$.

### 4.2.1 Sensitivity to cloud geometrical thickness as a function of cloud height

Having seen the effect of moving the same cloud vertically through the atmosphere, it is interesting to investigate the influence of a cloud to changes in its geometric thickness at a given height. To this end, clouds of optical thickness $\tau_{cloud} = 1$ and $\tau_{cloud} = 10$ and median droplet radius $r_0 = 5$ μm have

been considered, each at the six different top heights assumed in Sect. 4.2. The influence of cloud thickness at each of these levels on the reflected Stokes vector parameters $I$ and $Q$, both for the (optically) thin and thick cloud, is examined by varying the height of the cloud base to yield the geometric thicknesses $\Delta z = 200$ m and $\Delta z = 600$ m.

The upper panel of Fig. 8 shows the intensity response of changing the cloud thickness from 200 to 600 m with respect to cloud top height for different total column absorption strengths for, both, the optically thick (solid lines) and thin cloud (broken lines). In the absence of absorption, there is practically no sensitivity to both $z$ and $\Delta z$ (red lines coincide with $\Delta I = 0$). For absorbing lines, the response $\Delta I$ of optically thick clouds is stronger due to more scattering. At high absorption strengths, $\Delta I$ is sensitive to only high clouds (yellow and black lines representing $\tau_{abs,0} \approx 10$ and $\tau_{abs,0} \approx 30$, respectively). However, for moderate absorption strengths where $\tau_{abs,0} \lesssim 5$, the sensitivity to cloud geometric thickness attains a maximum at an intermediate cloud height, which increases with increasing absorption strength. The sensitivity of $I$ to $\Delta z$ varies with cloud height on two accounts.

1. Low clouds see a larger gradient of the air mass profile, leading to larger changes with increasing geometric thickness in the amount of both Rayleigh scattering as well as $O_2$ absorption. This contributes to the higher sensitivity to $\Delta z$ for absorbing lines that are not already saturated before the light reaches the low cloud.

2. However, light reflected back by low clouds undergoes more intermediate extinction by overlying atmospheric layers than that coming from higher clouds. This lowers the sensitivity with increasing $\tau_{abs,0}$.

These two opposing effects cause a maximum sensitivity to geometric thickness at an intermediate absorption strength for most clouds. This optimal absorption strength increases with increasing cloud height. Thus, in the case of the optically thick cloud shown in Fig. 8, for example, maximum sensitivity of $I$ to cloud geometric thickness occurs near $z = 6$ km for $\tau_{abs,0} \approx 1$ (solid blue line), while an absorption strength of $\tau_{abs,0} \approx 5$ (solid violet line) is most sensitive to geometric thicknesses of clouds near $z = 8$ km.

While the sensitivity of $I$ is larger for the optically thicker cloud, the lower panel of Fig. 8 shows that $Q$ is more sensitive to $\Delta z$ for optically thinner clouds. This is not surprising, given that $Q$ depends only on the first few orders of scattering. These occur predominantly only near the cloud top for optically thick clouds, so that light emerging from lower depths of the cloud have practically no effect on $Q$. For optically thinner clouds, there is enough low-order scattering occurring throughout the vertical extent of the cloud, leading to a higher sensitivity of $Q$ to $\Delta z$.

The red lines in the lower panel of Fig. 8 show that $Q$ increases with increasing $\Delta z$ in the absence of absorption.
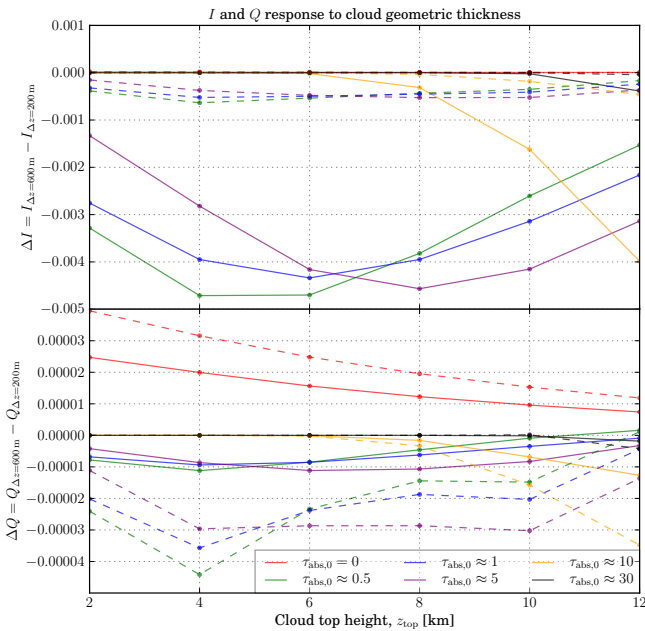
**Figure 8.** Height dependence of the change in intensity $\Delta I$ (upper panel) and of $\Delta Q$ (lower panel) due to a change in cloud thickness from $\Delta z = 200$ m to $\Delta z = 600$ m for different total column absorption strengths (represented by different line colors). The solid lines represent a thick cloud of optical depth $\tau_{\text{cloud}} = 10$, while broken lines show a thin cloud of optical depth $\tau_{\text{cloud}} = 1$.

As also explained in Sect. 4.2, this is because scattering at deeper atmospheric layers allows for a larger contribution to $Q$ due to Rayleigh scattering. This effect is reversed by increased extinction at deeper scattering levels in the presence of absorption, so that all the lines considered here with $\tau_{\text{abs},0} > 0$ lie above $\Delta Q = 0$, except the highest cloud (both optically thin and thick) at $z = 12$ km at low absorption strength, viz., $\tau_{\text{abs},0} \approx 0.5$ (dashed and solid green lines).

The sensitivity of $\Delta Q$ to $\Delta z$ is governed by the same opposing effects as that of $\Delta I$. However, the dependence on only low orders of scattering leads to the emergence of two distinct peaks (the first dominated by more Rayleigh scattering, and the second by scattering due to cloud droplets) in $\Delta Q$ with respect to cloud height $z$ for the optically thin cloud at $\tau_{\text{abs},0} \approx 0.5$ (dashed green line), $\tau_{\text{abs},0} \approx 1$ (dashed blue line) and $\tau_{\text{abs},0} \approx 5$ (dashed violet line).

## 4.3   Sensitivity to cloud droplet size

The upper panels of Fig. 7 show limited variation in $I$ due to droplet size, remaining well bound between the lower limit of Rayleigh scattering and an upper limit set by the WLP at 6.4 km.

For non-absorbing wavelengths in the geometry considered here, the dependence on $r_0$ appears to be limited to the increase in isotropicity (and hence a scattering component at wider angles of scattering) with decreasing droplet size. This

also explains the spectral response of $Q$ shown in the lower panels of Fig. 7. In both cases, the response is strongest in the absence of absorption, and non-linear with respect to droplet size $r_0$.

While Fig. 7 shows a weak sensitivity to droplet size at the view geometry considered, the dependence of the phase matrix on particle size, as described in Sect. 3, suggests a greater sensitivity of the angular details of $I$ and $Q$ to $r_0$. This information is exploited by multi-angle, polarization-sensitive measurements by instruments like POLDER (Deschamps et al., 1994, Polarization and Directionality of the Earth's Reflectances;), RSP (Research Scanning Polarimeter; Cairns et al., 1999), APS (Aerosol Polarimetry Sensor; Peralta et al., 2007), MSPI (Multi-angle Spectro Polarimetric Imager; Diner et al., 2008), and the future instrument 3MI (Multi-viewing Multi-channel Multi-polarisation Imager; Manolis et al., 2013). As noted by Boesche et al. (2009) and Frankenberg et al. (2012), the target mode of the OCO-2 instrument could allow using the sensitivity of multi-angle measurements of $I$ and $Q$ to $r_0$ through the phase matrix. While the instrument slit remains perpendicular to the principal plane during OCO-2 Nadir and Glint mode observations resulting in measurements of $\frac{1}{2}(I + Q)$ over the O$_2$ A band, Target mode observations depart from the principal plane, resulting in measurements of a linear combination of the Stokes components, $\frac{1}{2}(I + \cos 2\phi_{\text{pp}} Q + \sin 2\phi_{\text{pp}} U)$, that depends on the angle $\phi_{\text{pp}}$ made by the slit with the principal plane. GOSAT measurements, which are carried out at a view angle that roughly varies between $\pm 35°$, also offer multi-angle capabilities that could be combined with its more comprehensive polarimetric coverage (measuring two orthogonal components $I_{\text{P}}$ and $I_{\text{S}}$ as introduced in Sect. 1) to obtain more information on cloud droplet size.

The sensitivity of multi-angle sampling of $I$ and $Q$ to cloud droplet size is examined in more detail in the following section.

### 4.3.1   Angular dependence of the droplet size sensitivity of the O$_2$ A band

In order to examine the angular dependence of the sensitivity of the O$_2$ A band to droplet size, we simulate the Stokes components $I$ and $Q$ within the principle plane containing the Sun at a fixed zenith angle of $\theta_0 = 60°$ and nine view zenith angles – $\theta_{\text{view}} = -70.5, -60, -45.6, -26.1, 0, 26.1, 45.6, 60,$ and $70.5°$ – as in the MISR instrument (Multi-angle Imaging SpectroRadiometer; Diner et al., 1998). Using a non-absorbing wavelength (750 nm) near the A band, simulations of $I$ and $Q$ are made at all nine view angles for optically thin ($\tau_{\text{cloud}} = 1$) and thick ($\tau_{\text{cloud}} = 10$) clouds. For the optically thin cloud, Fig. 10 shows the multi-angle simulations of $I$ in the left panel, while the Stokes vector $Q$ and the corresponding degree of linear polarization $p = |Q|/I$ are shown in the upper

and lower right panels. The corresponding simulations for the optically thick cloud are depicted in Fig. 11.

Due to the assumption of a common cloud optical thickness in both the thin and thick cloud cases, the discussion of Sect. 3 indicates that the signals $I$ and $Q$ each depend on the size $r_0$ only through the scattering matrix $\mathbf{F}(\theta_{\text{scatt}})$, where the scattering angle $\theta_{\text{scatt}}$ is related to the view angle $\theta_{\text{view}}$ as

$$\theta_{\text{scatt}} = \cos^{-1}\left\{\sin\theta_0 \sin|\theta_{\text{view}}|\cos(\phi_{\text{view}} - \phi_0) - \cos\theta_0\cos|\theta_{\text{view}}|\right\}. \quad (9)$$

In the above equation, the solar zenith angle is measured such that $0° \leq \theta_0 < 90°$. $\phi_0 = 0°$ and $\phi_{\text{view}}$ are the solar and view azimuth angles, respectively. View angles at which the Sun is behind the detector are denoted by $\theta_{\text{view}} < 0$ (with $\phi_{\text{view}} = 180°$ in the principal plane), otherwise $\theta_{\text{view}} \geq 0$ (with $\phi_{\text{view}} = 0°$ in the principal plane).

Due to the single scatter relation $\mathbf{I} = \mathbf{F} \cdot \mathbf{I_0}$, where $\mathbf{I} = [I, Q, U, V]^T$ and $\mathbf{I_0} = [1, 0, 0, 0]^T$ denote the scattered and incident Stokes vectors, the angular distribution of $I$ is governed by the element $F_{11}$ of the scattering matrix, while that of $Q$ (in a frame of reference attached to the scattering plane) is largely driven by the element $F_{21}$. $F_{11}$ and $F_{21}$ are related to $P_h$ and $P_v$ of Fig. 4 such that $F_{11} = F_{22} = \frac{1}{2}(P_h + P_v)$ while $F_{12} = F_{21} = \frac{1}{2}(P_h - P_v)$.

As a result of the above dependencies, the angular nature of the size dependence of the measured $I$ and $Q$, respectively, can be expected to be related to the form of $F_{11}$ and $F_{21}$ corresponding to the view angles ($\theta_{\text{view}}$), as shown in Fig. 9.

### 4.3.2 Angular sensitivity of $I$ to droplet size $r_0$

It is evident from the left panels of both Figs. 10 and 11 that the intensity of light reflected back by the optically thicker cloud is greater at all angles. In each case, the reflected $I$ due to Rayleigh scattering alone (blue line) is depicted as a reference. In the absence of absorption, the reflectance due to the WLP is simply $1/\pi$ at all angles and hence has not been shown.

In both cases, the forward scatter directions ($\theta_{\text{view}} > 0$) show higher intensities than backscatter directions ($\theta_{\text{view}} < 0$), attributable to the strongly asymmetric nature of the cloud phase function which strongly favors scattering in the forward hemisphere (see Fig. 9, left panel), and the consequently increased multiple scattering observed at scattering angles smaller than 90°.

The nadir view angle, $\theta_{\text{view}} = 0°$, corresponds in the geometry considered here to a scattering angle $\theta_{\text{scatt}} = 120°$, at which both $P_h$ and $P_v$ in Fig. 4 as well as $F_{11}$ in Fig. 9 can be seen to have diminished sensitivity to droplet size. This sensitivity, however, increases away from $\theta_{\text{scatt}} = 120°$ in both directions for $F_{11}$, which drives the angular distribution of the total intensity $I$. This is reflected in the behavior of $I$ in the vicinity of the nadir view angle for the low cloud optical thickness case in both directions (both $\theta_{\text{view}} \lesssim 0$ and $\theta_{\text{view}} \gtrsim 0$) as well as for $\theta_{\text{view}} \lesssim 0$ in the high cloud optical thickness
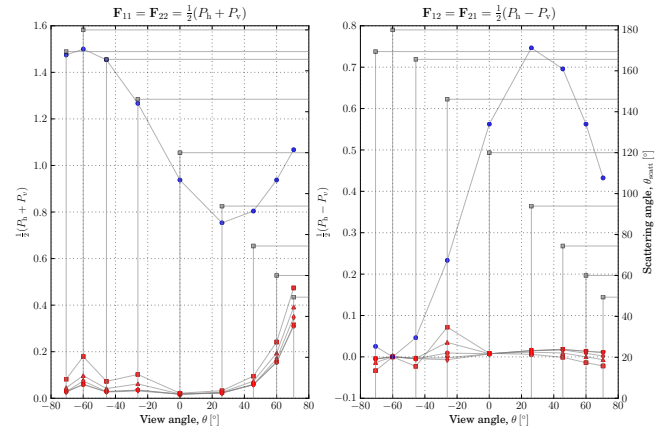


**Figure 9.** Elements $F_{11}$ (left panel) and $F_{21}$ (right panel) of the scattering matrix $\mathbf{F}(\theta_{\text{scatt}})$ for Rayleigh scattering (blue circles) as well as due to different cloud droplet sizes shown in red using different marker shapes (a square for $r_0 = 5\,\mu\text{m}$, a triangle pointing up for $r_0 = 7.5\,\mu\text{m}$, a circle for $r_0 = 10\,\mu\text{m}$, a triangle pointing down for $r_0 = 12.5\,\mu\text{m}$ and a diamond for $r_0 = 15\,\mu\text{m}$). Given a solar zenith angle, $\theta_0 = 60°$, the scattering angle $\theta_{\text{scatt}}$ is shown on the right ordinate of each panel (grey squares) as a function of view angle within the principal plane.
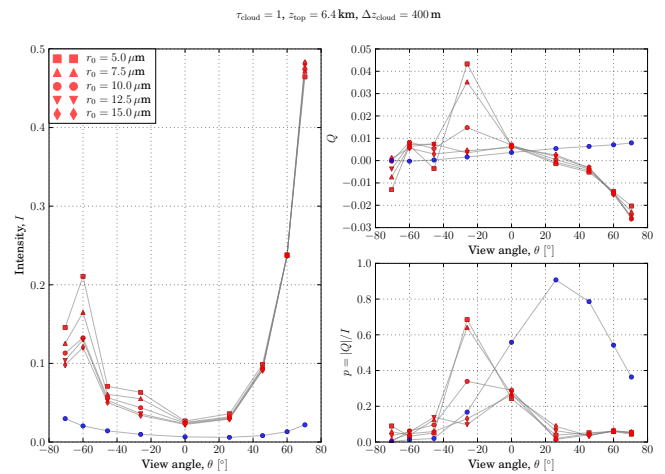


**Figure 10.** Simulated intensities $I$ (left), $Q$ (upper right) and $p$ (lower right) with respect to $\theta_{\text{view}}$ for clouds of optical thickness $\tau_{\text{cloud}} = 1$ and of varying droplet size $r_0 = 5, 7.5, 10, 12.5,$ and $15\,\mu\text{m}$ at 750 nm ($\tau_{\text{abs},0} = 0$).

case. At higher $|\theta_{\text{view}}|$, however, $F_{11}$ alone cannot explain the angular sensitivity of $I$ to $r_0$.

For the backscatter angles ($\theta_{\text{view}} < 0$), the sensitivity to $r_0$ of the scattered intensities closely resembles the size dependence of the phase function, revealing a largely low-order scattering signal. As a result, this angular range is well suited to the detection of droplet size, with good resolution near the angle of exact backscattering $\theta_{\text{scatt}} = 180°$
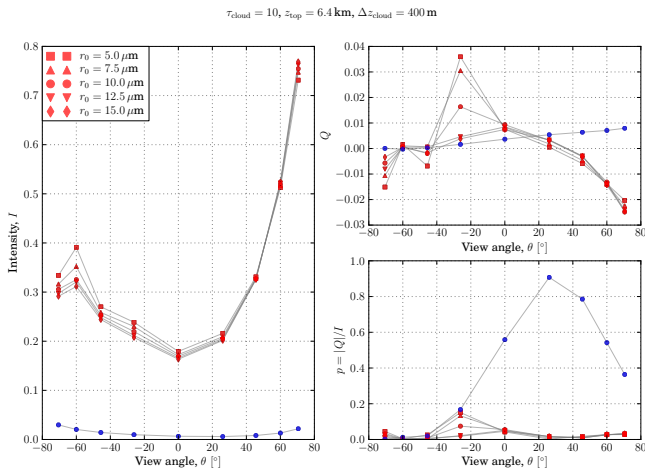
**Figure 11.** Same as Fig. 10 except that the Stokes component $I$ is shown for a cloud of optical thickness of $\tau_{cloud} = 10$.

occurring at $\theta_{view} = -60°$ and at the rainbow occurring near $\theta_{scatt} = 146.1°$, seen at $\theta_{view} = -26.1°$.

At larger forward scatter angles ($\theta_{view} \gg 0$), however, the size dependence of the intensity either diminishes with increasing $\theta_{view}$ or becomes reversed (diamonds at the top, squares at the bottom). The high order of multiple scattering within the forward peak causes the original size dependence of the scattered signal to be blurred. Smaller droplets (e.g., the smallest $r_0 = 5 \mu m$ represented by squares) show a more isotropic distribution of light than larger ones (e.g., the largest $r_0 = 15 \mu m$ represented by diamonds), leading to a greater intensity spread around the forward peak but less concentration within the forward peak for smaller droplets and vice versa.

This "convolution" due to multiple scattering causes the reversal in the size sensitivity at large positive view angles and generally diminished size sensitivity: increasing cloud optical thickness gives rise to more multiple scattering and thus greater mixing of the forward peak at $\theta_{scatt} = 0°$ (stronger for larger droplets) with surrounding angular regions at $0° \lesssim \theta_{scatt} < 90°$ (stronger for smaller droplets). These angular regions are represented by the positive view angles of the geometry chosen in this study. As a result, small droplets dominate the scattered signal in the low-order scattering regime due to less mixing between the forward peak and the rest of the angular range, while larger droplets dominate the strongly multiply scattered signal. Intermediate orders of scattering, e.g., at larger positive angles in the thin cloud case, do not show a clear dependence on size.

### 4.3.3 Angular sensitivity of $Q$ to droplet size $r_0$

The upper right panels of Figs. 10 and 11 show that, contrary to the case of $I$, $Q$ is often slightly larger in the case of the optically thin cloud or nearly equal owing to more low-order scattering, especially at the backscatter angles ($\theta_{view} < 0$).

Excepting the direction of exact backscatter (where $Q = 0$), the entire backscatter region ($\theta_{view} < 0$) is more sensitive to droplet size than the forward scatter angles ($\theta_{view} > 0$). The strongest resolution of particle size, however, occurs at the rainbow, which can be observed near $\theta_{scatt} = 146.1°$ at $\theta_{view} = -26.1°$.

As in the case of $F_{11}$ for $I$, the very low values of $F_{21}$ (see Fig. 9) for all cloud droplet sizes considered here at $\theta_{scatt} = 120°$, coincident with the nadir view angle $\theta_{view} = 0°$, makes the nadir $Q$ signal insensitive to droplet size for both the optically thin and thick cloud.

### 4.3.4 Significance for multi-angular spectropolarimetric remote sensing of cloud microphysics

It is clear that the backscatter region contains information on droplet size, both in the $I$ and the $Q$ components of the Stokes vector. Most of the information in the $I$ signal is contained at the exact backscatter angle ($\theta_{scatt} = 180°$), while there is no significant contribution from $Q$ at this angle. In the rest of the glory region ($\theta_{scatt} \lesssim 180°$), however, $Q$ has a significant negative contribution, so that $I_v = \frac{1}{2}(I - Q)$ would be more sensitive to droplet size than $I$ alone, which in turn would be more sensitive than $I_h = \frac{1}{2}(I + Q)$. In the rainbow region ($\theta_{scatt} = 146.1°$, $\theta_{view} = -26.1°$), however, $Q$ has a strong positive signal, so that $I_h = \frac{1}{2}(I + Q)$ would carry maximum information on droplet size compared to $I$ alone or $I_v = \frac{1}{2}(I - Q)$.

In our example, where the Sun is assumed to be at a zenith angle $\theta_0 = 60°$, the nadir geometry alone would be a relatively poor source of information on droplet size. Multi-angle measurements provide the flexibility to choose geometries that are rich in information, leading to potentially more accurate retrievals.

When the Sun is not close to zenith, the forward-scatter part ($\theta_{view} > 0$) of a multi-angle swath is relatively poor in its ability to provide information on the droplet size of clouds, mainly because the predominant source of the measured signal is multiple scattering. This is also expected for brighter, nearly isotropically reflecting surfaces, even though the simulations shown here have been made for a black surface. The only exception would be a specular surface (like a relatively calm ocean) in the Sun glint region, where the forward peak can be strong enough to retain information on the droplet size (Sanghavi et al., 2013, 2014). Further, it should be noted that the decreasing sensitivity to lower atmospheric layers and the ground surface in the presence of absorption is useful to determine the optical thickness of a cloud even in the absence of sufficient information about the brightness of the ground surface.

## 5 Distinguishability of the cloud parameters $\tau_{cloud}$, $z_{top}$ and $r_0$

The previous section dealt with the sensitivity of intensity and polarization to different cloud parameters, treated individually in cases where all other parameters were held fixed. This helped to identify different characteristic sensitivities of $I$ and $Q$ in different parts of the $O_2$ A band to each of the three main cloud parameters of interest, viz., $\tau_{cloud}$, $z_{top}$ and $r_0$. This differential sensitivity, qualitatively summarized in Table 1 can be useful for a simultaneous retrieval of all three parameters in an optimal estimation setup (Rodgers, 2000), where $\tau_{cloud}$, $z_{top}$ and $r_0$ form part of the state vector $\mathbf{x}$, with the measurement vector given by hyperspectral measurements of the $O_2$ A band. Table 1 makes it obvious that polarimetric and multi-angle data would add important information to such a measurement, making it easier to clearly distinguish the different retrieved parameters. Such a study, making use of Jacobian matrices and instrumental noise statistics for quantitative information content and error analyses will be the subject of a follow-up study.

## 6 Conclusions

We derive a bivariate sensitivity of light reflected by the $O_2$ A band to the total atmospheric absorption strength and the height of scattering above the surface. This intrinsic sensitivity, combined with the optical thickness and the droplet size dependence of the phase matrix of a pure water cloud, is shown to determine the characteristic Stokes vector of light reflected back by clouds. We have studied the polarimetric response of the $O_2$ A band as measured by instruments like GOSAT and OCO-2 to three important cloud parameters, viz., optical thickness, top height and droplet size, by simulating changes in the measured signal with respect to changes in each parameter, with everything else kept constant. We identify the following distinct patterns in the $O_2$ A-band response to each parameter.

1. For optically thick clouds, the intensity $I$ was sensitive to the cloud optical thickness, but $Q$ showed negligible sensitivity, both for strong and weak absorption.

2. In the absence of absorption, there is no sensitivity of $I$ to cloud height, while $Q$ shows maximum sensitivity. In the presence of absorption, both $I$ and $Q$ are sensitive to the height of the cloud.

3. The sensitivity to cloud droplet size is dependent on the scene geometry, with maximum sensitivity for both $I$ and $Q$ at non-absorbing wavelengths.

These distinct responses to the three parameters can be expected to help identify the contributions of each to a measurement. This suggests that it should be possible to carry out

**Table 1.** Characteristic sensitivity of the $O_2$ A band to cloud optical thickness, top height and droplet size.

| Parameter | $I_{\tau_{abs,0}=0}$ | $I_{\tau_{abs,0}>0}$ | $Q_{\tau_{abs,0}=0}$ | $Q_{\tau_{abs,0}>0}$ |
|---|---|---|---|---|
| $\tau_{cloud}$ | yes | yes | no[a] | no[a] |
| $z_{top}$ | no | yes | yes | yes |
| $r_0$ | yes[b] | no[c] | yes[b] | no[c] |

[a] for high $\tau_{cloud}$. [b] shows strong angular dependence. [c] weaker sensitivity than at $\tau_{abs,0} = 0$.

simultaneous retrievals of these parameters from polarimetric hyperspectral measurements using methods like optimal estimation.

The dependence of the sensitivity of $I$ and $Q$ to cloud geometric thickness on cloud top height and total atmospheric absorption has also been examined. Our study suggests that maximum sensitivity to cloud height occurs at stronger atmospheric absorption as the cloud top height increases.

Since the sensitivity of measurements to droplet size were found to be strongly dependent on scene geometry, it is proposed to use multi-angle measurements such as those available from the Target mode for OCO-2 to better constrain the cloud droplet size. The best sensitivity to droplet size was obtained for measurements of $I$ at and near the exact backscatter angle followed by the rainbow region. For $Q$, maximum sensitivity was obtained near the rainbow at a scattering angle of $\sim 146°$, followed by angles close to but not including the exact backscatter direction.

## References

Abreu, L. and Anderson, G.: The MODTRAN 2/3 report and LOW-TRAN 7 model, Contract, 19628, 0132, 1996.

Ackerman, S., Holz, R., Frey, R., Eloranta, E., Maddux, B., and McGill, M.: Cloud detection with MODIS. Part II: validation, J. Atmos. Ocean. Tech., 25, 1073–1086, 2008.

Anderson, G. P., Clough, S., Kneizys, F., Chetwynd, J., and Shettle, E. P.: AFGL atmospheric constituent profiles (0.120 km), Tech. rep., DTIC Document, 1986.

Baker, M.: Cloud microphysics and climate, Science, 276, 1072–1078, 1997.

Bodhaine, B. A., Wood, N. B., Dutton, E. G., and Slusser, J. R.: On Rayleigh optical depth calculations., J. Atmos. Ocean. Tech., 16, 1854–1861, 1999.

Boesche, E., Stammes, P., and Bennartz, R.: Aerosol influence on polarization and intensity in near-infrared $O_2$ and $CO_2$ absorption bands observed from space, J. Quant. Spectrosc. Ra., 110, 223–239, 2009.

Bohren, C. F. and Huffman, D. R.: Absorption and scattering of light by small particles, Wiley, New York, 1983.

Cairns, B., Russell, E. E., and Travis, L. D.: Research scanning polarimeter: calibration and ground-based measurements, in: SPIE's International Symposium on Optical Science, Engineering, and Instrumentation, International Society for Optics and Photonics, 186–196, 1999.

Chahine, M. T.: The hydrological cycle and its influence on climate, Nature, 359, 373–380, 1992.

Crisp, D., Atlas, R., Breon, F.-M., Brown, L., Burrows, J., Ciais, P., Connor, B., Doney, S., Fung, I., Jacob, D., Miller, C., O'Brien, D., Pawson, S., Randerson, J., Rayner, P., Salawitch, R., Sander, S., Sen, B., Stephens, G., Tans, P., Toon, G., Wennberg, P., Wofsy, S., Yung, Y., Kuang, Z., Chudasama, B., Sprague, G., Weiss, B., Pollock, R., Kenyon, D., and Schroll, S.: The orbiting carbon observatory (OCO) mission, Adv. Space Res., 34, 700–709, 2004.

Deirmendjian, D.: Electromagnetic Radiation Scattering by Spherical Polydispersed Particles, Elsevier, New York, 1969.

Deschamps, P.-Y., Bréon, F.-M., Leroy, M., Podaire, A., Bricaud, A., Buriez, J.-C., and Seze, G.: The POLDER mission: Instrument characteristics and scientific objectives, IEEE T. Geosci. Remote, 32, 598–615, 1994.

Dessler, A., Palm, S., and Spinhirne, J.: Tropical cloud-top height distributions revealed by the Ice, Cloud, and Land Elevation Satellite (ICESat)/Geoscience Laser Altimeter System (GLAS), J. Geophys. Res.-Atmos., 111, D12215, doi:10.1029/2005JD006705, 2006.

Diner, D. J., Beckert, J. C., Reilly, T. H., Bruegge, C. J., Conel, J. E., Kahn, R. A., Martonchik, J. V., Ackerman, T. P., Davies, R., Gerstl, S. A., Gordon, H., Muller, J.-P., Myneni, R., Sellers, P., Pinty, B., and Verstraete, M.: Multi-angle Imaging SpectroRadiometer (MISR) instrument description and experiment overview, IEEE T. Geosci. Remote, 36, 1072–1087, 1998.

Diner, D. J., Mischna, M., Chipman, R. A., Davis, A., Cairns, B., Davies, R., Kahn, R. A., Muller, J.-P., and Torres, O.: WindCam and MSPI: two cloud and aerosol instrument concepts derived from Terra/MISR heritage, in: Society of Photo-Optical Instrumentation Engineers (SPIE) Conference Series, vol. 7081, p. 25, 2008.

Fischer, J. and Grassl, H.: Detection of cloud-top height from backscattered radiances within the oxygen A band. Part 1: Theoretical study, J. Appl. Meteorol., 30, 1245–1259, 1991.

Fischer, J., Cordes, W., Schmitz-Peiffer, A., Renger, W., and Mörl, P.: Detection of cloud-top height from backscattered radiances within the oxygen A band. Part 2: Measurements, J. Appl. Meteorol., 30, 1260–1267, 1991.

Fowler, L. D., Randall, D. A., and Rutledge, S. A.: Liquid and ice cloud microphysics in the CSU general circulation model. Part 1: Model description and simulated microphysical processes, J. Climate, 9, 489–529, 1996.

Frankenberg, C., Hasekamp, O., O'Dell, C., Sanghavi, S., Butz, A., and Worden, J.: Aerosol information content analysis of multi-angle high spectral resolution measurements and its benefit for high accuracy greenhouse gas retrievals, Atmos. Meas. Tech., 5, 1809–1821, doi:10.5194/amt-5-1809-2012, 2012.

Gómez-Chova, L., Camps-Valls, G., Amorós-López, J., Guanter, L., Alonso, L., Calpe, J., and Moreno, J.: New cloud detection algorithm for multispectral and hyperspectral images: Application to ENVISAT/MERIS and PROBA/CHRIS sensors, in: IEEE International Geoscience and Remote Sensing Symposium, IGARSS, 2757–2760, 2006.

Hamazaki, T., Kaneko, Y., Kuze, A., and Kondo, K.: Fourier transform spectrometer for greenhouse gases observing satellite (GOSAT), in: Fourth International Asia-Pacific Environmental Remote Sensing Symposium 2004: Remote Sensing of the Atmosphere, Ocean, Environment, and Space, International Society for Optics and Photonics, 73–80, 2005.

Hasekamp, O. P. and Butz, A.: Efficient calculation of intensity and polarization spectra in vertically inhomogeneous scattering and absorbing atmospheres, J. Geophys. Res.-Atmos., 113, 20309, doi:10.1029/2008JD010379, 2008.

Heidinger, A. K. and Stephens, G. L.: Molecular line absorption in a scattering atmosphere. Part II: Application to remote sensing in the $O_2$ A band, J. Atmos. Sci., 57, 1615–1634, 2000.

Hovenier, J.: Multiple scattering of polarized light in planetary atmospheres, Astron. Astrophys., 13, 7, 1971.

Key, J. and Barry, R.: Cloud cover analysis with Arctic AVHRR data: 1. Cloud detection, J. Geophys. Res.-Atmos., 94, 18521–18535, 1989.

Koelemeijer, R. B., Stammes, P., Hovenier, J., and de Haan, J.: A fast method for retrieval of cloud parameters using oxygen A band measurements from the Global Ozone Monitoring Experiment, J. Geophys. Res.-Atmos., 106, 3475–3490, 2001.

Kokhanovsky, A. A.: Cloud optics, vol. 34, Springer, 2006.

Kuze, A. and Chance, K. V.: Analysis of cloud top height and cloud coverage from satellites using the $O_2$ A and B bands, J. Geophys. Res.-Atmos., 99, 14481–14491, 1994.

Kuze, A., Suto, H., Nakajima, M., and Hamazaki, T.: Thermal and near infrared sensor for carbon observation Fourier-transform spectrometer on the Greenhouse Gases Observing Satellite for greenhouse gases monitoring, Appl. Optics, 48, 6716–6733, 2009.

Lohmann, U. and Feichter, J.: Impact of sulfate aerosols on albedo and lifetime of clouds: A sensitivity study with the ECHAM4 GCM, J. Geophys. Res.-Atmos., 102, 13685–13700, 1997.

Lohmann, U., Stier, P., Hoose, C., Ferrachat, S., Kloster, S., Roeckner, E., and Zhang, J.: Cloud microphysics and aerosol indirect effects in the global climate model ECHAM5-HAM, Atmos. Chem. Phys., 7, 3425–3446, doi:10.5194/acp-7-3425-2007, 2007.

Manolis, I., Grabarnik, S., Caron, J., Bézy, J.-L., Loiselet, M., Betto, M., Barré, H., Mason, G., and Meynart, R.: The MetOp second generation 3MI instrument, in: SPIE Remote Sensing, 88890J–88890J, International Society for Optics and Photonics, 2013.

Mayer, B., Schröder, M., Preusker, R., and Schüller, L.: Remote sensing of water cloud droplet size distributions using the backscatter glory: a case study, Atmos. Chem. Phys., 4, 1255–1263, doi:10.5194/acp-4-1255-2004, 2004.

Nakajima, T. and King, M. D.: Determination of the optical thickness and effective particle radius of clouds from reflected solar

radiation measurements. Part I: Theory, J. Atmos. Sci., 47, 1878–1893, 1990.

Nakajima, T., King, M. D., Spinhirne, J. D., and Radke, L. F.: Determination of the Optical Thickness and Effective Particle Radius of Clouds from Reflected Solar Radiation Measurements. Part II: Marine Stratocumulus Observations, J. Atmos. Sci., 48, 728–751, 1991.

Nakajima, T. Y. and Nakjma, T.: Wide-area determination of cloud microphysical properties from NOAA AVHRR measurements for FIRE and ASTEX regions, J. Atmos. Sci., 52, 4043–4059, 1995.

Nakajima, T. Y., Suzuki, K., and Stephens, G. L.: Droplet growth in warm water clouds observed by the A-Train. Part I: Sensitivity analysis of the MODIS-derived cloud droplet sizes, J. Atmos. Sci., 67, 1884–1896, 2010.

O'Brien, D. and Mitchell, R.: Error estimates for retrieval of cloud-top pressure using absorption in the A band of oxygen, J. Appl. Meteorol., 31, 1179–1192, 1992.

O'Brien, D. M., Polonsky, I., O'Dell, C., Kuze, A., Kikuchi, N., Yoshida, Y., and Natraj, V.: Testing the Polarization Model for TANSO-FTS on GOSAT Against Clear-Sky Observations of Sun Glint Over the Ocean, IEEE T. Geosci. Remote, 51, 5199–5209, 2013.

Peng, Y. and Lohmann, U.: Sensitivity study of the spectral dispersion of the cloud droplet size distribution on the indirect aerosol effect, Geophys. Res. Lett., 30, 1507, doi:10.1029/2003GL017192, 2003.

Peralta, R. J., Nardell, C., Cairns, B., Russell, E. E., Travis, L. D., Mishchenko, M. I., Fafaul, B. A., and Hooker, R. J.: Aerosol polarimetry sensor for the Glory Mission, in: International Symposium on Multispectral Image Processing and Pattern Recognition, 67865L–67865L, International Society for Optics and Photonics, 2007.

Pfeilsticker, K., Erle, F., Funk, O., Veitel, H., and Platt, U.: First geometrical pathlengths probability density function derivation of the skylight from spectroscopically highly resolving oxygen A-band observations: 1. Measurement technique, atmospheric observations and model calculations, J. Geophys. Res.-Atmos., 103, 11483–11504, 1998.

Platnick, S. and Valero, F. P.: A validation of a satellite cloud retrieval during ASTEX, J. Atmos. Sci., 52, 2985–3001, 1995.

Pollock, R., Haring, R. E., Holden, J. R., Johnson, D. L., Kapitanoff, A., Mohlman, D., Phillips, C., Randall, D., Rechsteiner, D., Rivera, J., Rodriguez, J. I., Schwochert, M. A., and Sutin, B. M.: The Orbiting Carbon Observatory Instrument: performance of the OCO instrument and plans for the OCO-2 instrument, in: Remote Sensing, 78260W–78260W, International Society for Optics and Photonics, 2010.

Rodgers, C. D.: Inverse methods for atmospheric sounding: theory and practice, vol. 2, World scientific Singapore, 2000.

Rothman, L. S., Gordon, I. E., Barbe, A., Benner, D. C., Bernath, P. F., Birk, M., Boudon, V., Brown, L. R., Campargue, A., Champion, J.-P., Chance, K., Coudert, L., Dana, V., Devi, V., Fally, S., Flaud, J.-M., Gamache, R., Goldman, A., Jaquemart, D., Kleiner, I., Lacome, N., Lafferty, W., Mandin, J.-Y., Massie, S., Mikhailenko, S., Miller, C., Moazzen-Ahmadi, N., Naumenko, O., Nikitin, A., Orphal, J., Perevalov, V., Perrin, A., Predoi-Cross, A., Rinsland, C., Rotger, M., Simeckova, M., Smith, M., Sung,

K., and Tashkun, S.: The HITRAN 2008 molecular spectroscopic database, J. Quant. Spectrosc. Ra., 110, 533–572, 2009.

Rozanov, V. V. and Kokhanovsky, A. A.: Semianalytical cloud retrieval algorithm as applied to the cloud top altitude and the cloud geometrical thickness determination from top-of-atmosphere reflectance measurements in the oxygen A band, J. Geophys. Res.-Atmos., 109, D05202, doi:10.1029/2003JD004104, 2004.

Rozanov, V. V., Kokhanovsky, A. A., and Burrows, J. P.: The determination of cloud altitudes using GOME reflectance spectra: multilayered cloud systems, IEEE T. Geosci. Remote, 42, 1009–1017, 2004.

Sanghavi, S., Martonchik, J. V., Landgraf, J., and Platt, U.: Retrieval of the optical depth and vertical distribution of particulate scatterers in the atmosphere using O$_2$ A- and B-band SCIAMACHY observations over Kanpur: a case study, Atmos. Meas. Tech., 5, 1099–1119, doi:10.5194/amt-5-1099-2012, 2012.

Sanghavi, S., Davis, A. B., and Eldering, A.: vSmartMOM: A vector matrix operator method-based radiative transfer model linearized with respect to aerosol properties, J. Quant. Spectrosc. Ra., 133, 412–433, 2014.

Sanghavi, S. V., Martonchik, J. V., Davis, A. B., and Diner, D. J.: Linearization of a scalar matrix operator method radiative transfer model with respect to aerosol and surface properties, J. Quant. Spectrosc. Ra., 116, 1–16, 2013.

Sassen, K., Wang, Z., and Liu, D.: Global distribution of cirrus clouds from CloudSat/Cloud-Aerosol Lidar and Infrared Pathfinder Satellite Observations (CALIPSO) measurements, J. Geophys. Res.-Atmos., 113, D00A12, 2008.

Schutgens, N., Tilstra, L., Stammes, P., and Bréon, F.-M.: On the relationship between Stokes parameters Q and U of atmospheric ultraviolet/visible/near-infrared radiation, J. Geophys. Res.-Atmos., 109, D09205, doi:10.1029/2003JD004081, 2004.

Slingo, A.: Sensitivity of the Earth's radiation budget to changes in low clouds, Nature, 343, 49–51, 1990.

Slingo, A. and Slingo, J.: The response of a general circulation model to cloud longwave radiative forcing. I: Introduction and initial experiments, Q. J. Roy. Meteor. Soc., 114, 1027–1062, 1988.

Stephens, G.: Radiation profiles in extended water clouds. II: Parameterization schemes, J. Atmos. Sci., 35, 2123–2132, 1978.

Stephens, G. L.: Cloud feedbacks in the climate system: A critical review, J. Climate, 18, 237–273, 2005.

Stephens, G. L. and Platt, C.: Aircraft observations of the radiative and microphysical properties of stratocumulus and cumulus cloud fields, J. Climate and applied meteorology, 26, 1243–1269, 1987.

Stephens, G. L., Vane, D. G., Boain, R. J., Mace, G. G., Sassen, K., Wang, Z., Illingworth, A. J., O'Connor, E. J., Rossow, W. B., Durden, S. L., Miller, S., RT, A., Benedetti, A., and Mirescu, C.: The CloudSat mission and the A-Train: A new dimension of space-based observations of clouds and precipitation, B. Am. Meteorol. Soc., 83, 1771–1790, 2002.

Stephens, G. L., Vane, D. G., Tanelli, S., Im, E., Durden, S., Rokey, M., Reinke, D., Partain, P., Mace, G. G., Austin, R., Benedetti, A., and Mitrescu, C.: CloudSat mission: Performance and early science after the first year of operation, J. Geophys. Res.-Atmos., 113, D00A18, doi:10.1029/2008JD009982, 2008.

Tran, H. and Hartmann, J.-M.: An improved O$_2$ A band absorption model and its consequences for retrievals of photon paths and surface pressures, J. Geophys. Res.-Atmos., 113, 18104, doi:10.1029/2008JD010011, 2008.

van de Hulst, H. C.: Light scattering by small particles, Courier Dover Publications, New York, 1957.

Van Diedenhoven, B., Hasekamp, O., and Landgraf, J.: Retrieval of cloud parameters from satellite-based reflectance measurements in the ultraviolet and the oxygen A-band, J. Geophys. Res.-Atmos., 112, 15208, doi:10.1029/2006JD008155, 2007.

Wiscombe, W. J.: Improved Mie scattering algorithms, Appl. Optics, 19, 1505–1509, 1980.